Available online at www.sciencedirect.com
SCIENCE DIRECT®
PERGAMON
International Journal of Multiphase Flow 29 (2003) 271–289
International Journal of Multiphase Flow
www.elsevier.com/locate/ijmulflow

Laminar-to-turbulent fluid-particle flows in a human airway model

C. Kleinstreuer *, Z. Zhang

Department of Mechanical and Aerospace Engineering, North Carolina State University, Campus Box 7910 3211, Broughton Hall, Raleigh, NC 27695-7910 USA

Received 26 April 2002; received in revised form 20 October 2002

Abstract

As in many biomedical and industrial applications, gas–solid two-phase flow fields in a curved tube with local area constrictions may be laminar, transitional and/or turbulent depending upon the inlet flow rate and tube geometry. Assuming steady incompressible air flow and non-interacting spherical micron-particles, the laminar-to-turbulent suspension flow problem was solved for a human airway model using a commercial software with user-supplied pre- and post-processing programs. All flow regimes ($500 < Re_{local} < 10^4$) were captured with an low-Reynolds-number k–ω turbulence model. Considering different steady inspiratory flow rates ($15 \leqslant Q \leqslant 60$ l/min) and Stokes numbers, the three-dimensional simulation results show the following:

(i) The onset of turbulence after the constriction in the larynx can be clearly observed when the inspiratory flow rate changes from low-level breathing ($Q_{in} = 15$ l/min) to high-level breathing ($Q_{in} = 60$ l/min). The flow reattachment length in the trachea becomes shorter, the axial velocity profile becomes more blunt, and the secondary flow decays faster with the occurrence of transition to turbulence.
(ii) Particles follow the basic relationship between airflow and particle motion very well at the lower inspiratory flow rate ($Q_{in} = 15$ l/min); however, particle motion seems to be random and disperse, i.e., influenced by flow fluctuations in case of high inspiratory flow ($Q_{in} = 60$ l/min).
(iii) Turbulence can enhance particle deposition in the trachea near the larynx to some extent, but it is more likely to affect the deposition of smaller particles (say, $St < 0.06$) throughout the airway at relatively high flow rates ($Q_{in} = 30$ and 60 l/min) due to turbulent dispersion. However, the particle size and inhalation flow rate (i.e., Stokes number) are still the main factors influencing particle deposition when compared with turbulent dispersion alone.

* Corresponding author. Tel.: +1-919-515-5216; fax: +1-919-515-7968.
E-mail address: ck@eos.ncsu.edu (C. Kleinstreuer).
URL: http://www.mae.ncsu.edu/research/ck_CFPDlab/index.html.

0301-9322/03/$ - see front matter
PII: S0301-9322(02)00131-3

The methodology outlined can be readily applied to other two-phase flows undergoing changing flow regimes in complex tubular systems.

Keywords: Computational gas–solid two-phase flow; Internal laminar-to-turbulent flow modeling; Micro-particle distributions; Human oral airway model

1. Introduction

Internal gas–solid two-phase flow undergoing different flow regimes has numerous applications. The particle suspension flow may be laminar in a conduit inlet section and then, after a reduction in cross-sectional area, becomes turbulent. Examples include aerosol inhalation (Katz and Martonen, 1999), blood flow in stenosed vessels (Ku, 1997; Berger and Jou, 2000), and pneumatic transport in pipes (Molerus, 1996). For a given system, the local Reynolds number may vary from 100 to 10,000. Since standard turbulence models (e.g. k–ε, RNG k–ε, k–ω, etc.), as reviewed by Wilcox (1998), Papageorgakis and Assanis (1999); and Pope (2000), are inappropriate for laminar-to-turbulent two-phase flows, low-Reynolds-number (LRN) turbulence models (cf. Kral, 1998; Radmehr and Patankar, 2001) have to be considered. In a comparison study of four readily available turbulence models, Zhang and Kleinstreuer (2002a) showed that the LRN k–ω version for internal constant-density flows preserved fully laminar flows and captured transitional and turbulent flows in three-dimensional conduits with different local obstructions.

In this study, the focus is on the effects of changing flow regimes on air flow and micro-particle transport in a surrogate geometry representing the oral airways (i.e., mouth to trachea) considering different breathing rates. Previous analyses, employing the k–ε turbulence model, were lacking in validations with experiments (see Katz and Martonen, 1996, 1999; Li et al., 1996, 1998; for example) or failed to simulate the airflow and aerosol dynamics accurately (see Stapleton et al., 2000). Other studies considered only laminar flow in the human upper airways (see Yu et al., 1998; for example).

The tubular airway in this study consists of the oral cavity (mouth), pharynx, larynx and trachea as shown in Fig. 1. The pharynx connects the oral cavity with the laryngeal airways during breathing. The larynx is part of the upper respiratory tract between the pharynx and the trachea which has a complicated structure framed by cartilage and bounded by ligaments and muscles. The glottis (laryngeal aperture) is formed between two flaps of vocal folds inside the larynx as they project into the airways from both sides of the larynx. The free edges of the vocal folds can be drawn together or moved wide apart, i.e., changing the resistance to air flow during sound production.

The aim is to develop a relatively simple and representative oral airway geometry that can generate the equivalent "filtering efficiency" for micron-size particles as shown with complicated cast models, or observed via in vivo tests. Traditionally, the oral cavity/pharynx/larynx region is approximated as a 90°-bend with constant cross-sectional areas. However, Li et al. (1996) and

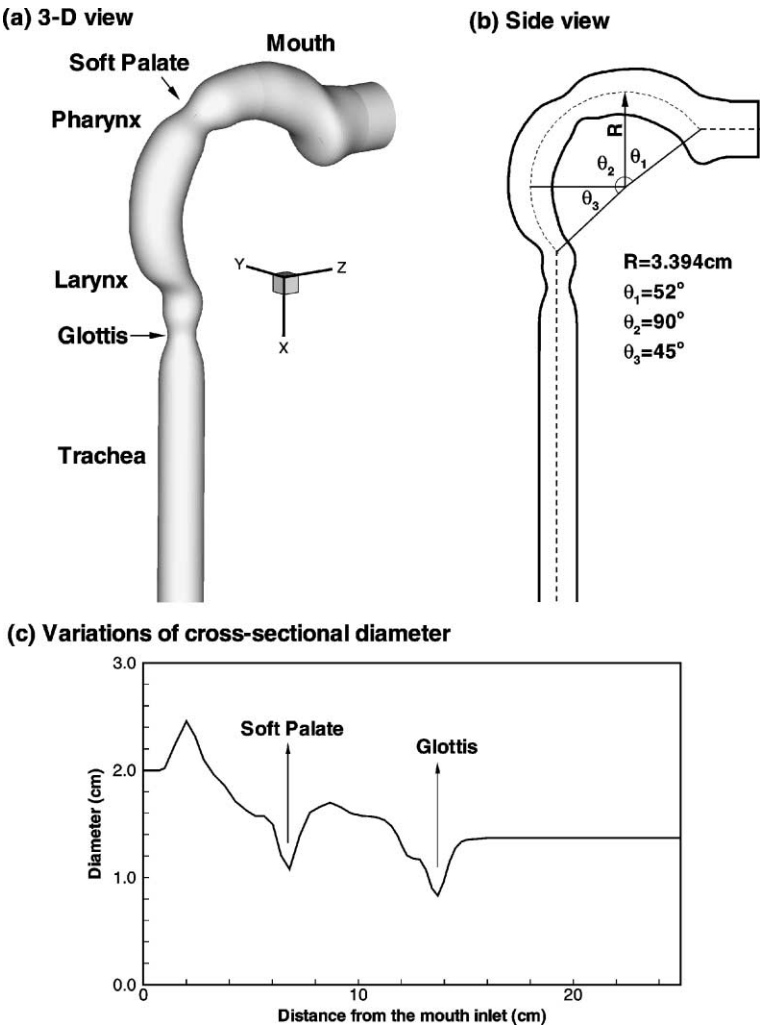

Fig. 1. Configuration of the oral airway model. The dimensions are based on data sets provided by Cheng et al. (1999) based on a human cast replica.

Cheng et al. (1999) have shown that large errors can be generated by employing such an over-simplified model when compared to measured data sets obtained with cast replicas. Therefore, a new surrogate geometry with variable circular cross-sections was developed in this study where the oral cavity/pharynx/larynx region is modeled as a near 180° curved bend (Fig. 1) as suggested by Cheng et al. (1999). The diameter variations along the oral airway from mouth to trachea are provided in Fig. 1(c), which are based on the hydraulic diameters measured from a replicate human oral airway cast of a healthy male adult with approximately 50 percent of full mouth opening (see Cheng et al., 1999). Variations to the actual cast also include a short mouth inlet with a diameter of 2 cm and a modified soft palate.

2. Theory

2.1. Governing equations

2.1.1. Airflow

In order to capture the air flow structures in the laminar-to-turbulent flow regimes, i.e., $500 < Re_{\text{local}} < 10^4$ for the present airway configuration and inhalation rates, the LRN k–ω model of Wilcox (1998) was selected and adapted for internal flow (cf. Zhang and Kleinstreuer, 2002a). Thus, the general transport equations in tensor notation, implying the double-index summation convention, read:

Continuity equation:

$$\frac{\partial \bar{u}_i}{\partial x_i} = 0 \tag{1}$$

Momentum equation:

$$\frac{\partial \bar{u}_i}{\partial t} + \bar{u}_j \frac{\partial \bar{u}_i}{\partial x_j} = -\frac{1}{\rho}\frac{\partial p}{\partial x_i} + \frac{\partial}{\partial x_j}\left[(\nu + \nu_T)\left(\frac{\partial \bar{u}_i}{\partial x_j} + \frac{\partial \bar{u}_j}{\partial x_i}\right)\right] \tag{2}$$

Turbulent kinetic energy (k) equation:

$$\frac{\partial k}{\partial t} + \bar{u}_j \frac{\partial k}{\partial x_j} = \tau_{ij}\frac{\partial \bar{u}_i}{\partial x_j} - \beta^* k\omega + \frac{\partial}{\partial x_j}\left[(\nu + \sigma_k \nu_T)\frac{\partial k}{\partial x_j}\right] \tag{3}$$

Pseudo-vorticity (ω) equation

$$\frac{\partial \omega}{\partial t} + \bar{u}_j \frac{\partial \omega}{\partial x_j} = \alpha\frac{\omega}{k}\tau_{ij}\frac{\partial \bar{u}_i}{\partial x_j} - \beta\omega^2 + \frac{\partial}{\partial x_j}\left[(\nu + \sigma_\omega \nu_T)\frac{\partial \omega}{\partial x_j}\right] \tag{4}$$

where the turbulent viscosity is given as $\nu_T = c_\mu f_\mu k/\omega$, and the function f_μ is defined as $f_\mu = \exp[-3.4/(1 + R_T/50)^2]$ with $R_T = \rho k/(\mu\omega)$. ρ, ν, and μ are density, kinetic viscosity, and dynamic viscosity of the air, respectively. The other coefficients in the above equations are

$$C_\mu = 0.09, \quad \alpha = 0.555, \quad \beta = 0.8333, \quad \beta^* = 1, \quad \sigma_k = \sigma_\omega = 0.5 \tag{5a–f}$$

Presently, the steady 3-D form of Eqs. (2)–(4) has been solved where the time derivatives are equal to zero.

2.1.2. Particle transport

In light of the large particle-to-air density ratio, dilute monodisperse particle suspensions, and negligible particle rotation, drag is the dominant point force. Hence, the particle trajectory equation can be written as

$$\frac{\mathrm{d}}{\mathrm{d}t}(m_\mathrm{p} u_i^\mathrm{p}) = \frac{1}{8}\pi\rho d^2 C_\mathrm{Dp}(u_i - u_i^\mathrm{p})|u_j - u_j^\mathrm{p}| \tag{6}$$

where u_i^p and m_p is the velocity and mass of the particle, respectively; C_Dp is the drag force coefficient given by

$$C_{\mathrm{Dp}} = C_{\mathrm{D}}/C_{\mathrm{slip}} \tag{7}$$

where

$$C_{\mathrm{D}} = \begin{cases} 24/Re_{\mathrm{p}} & \text{for } 0.0 < Re_{\mathrm{p}} \leqslant 1.0 \\ 24/Re_{\mathrm{p}}^{0.646} & \text{for } 1.0 < Re_{\mathrm{p}} \leqslant 400 \end{cases} \tag{8}$$

and the particle Reynolds number is

$$Re_{\mathrm{p}} = \rho |u_j - u_j^{\mathrm{p}}| d/\mu \tag{9}$$

A correlation for the Cunningham correction (i.e., slip) factor, C_{slip}, in Eq. (7) can be found in Clift et al. (1978). Here, u_i is the instantaneous fluid velocity with $u_i = \bar{u}_i + u_i'$, where $\bar{u}_i$ is the time-averaged or bulk velocity of the fluid, and u_i' is its fluctuating component which can be expressed as (Gosman and Ioannides, 1981; Katz and Martonen, 1999):

$$u_i' = \lambda \left(\frac{2}{3} k_i \right)^{1/2} \tag{10}$$

Thus, the stochastic nature of turbulence is modeled as the product of time-averaged turbulence energy and a random number λ with zero-mean, variance of one and Guassian distribution.

The associated boundary conditions include uniform velocity profiles and particle distributions prescribed at the inlet, and zero pressure at the outlet. The initial particle velocities were set equal to that of the fluid and one-way coupling was assumed between the air and particle flow fields. At the inlet, the initial values for k, and ω were assigned using the following empirical relation (Kral, 1998; AEA Technology, 2001);

$$k = 1.5(I_{\mathrm{in}} u_{\mathrm{in}})^2, \quad \text{and} \quad \omega = \frac{k^{0.5}}{0.3D} \tag{11}$$

where, u_{in} is the mean-velocity at the inlet, I_{in} is the inlet turbulence intensity usually taken as 0.037 (AEA Technology (2001)) and D is the diameter of the inlet tube. The sensitivity of mean flow fields and turbulence kinetic energy in the model to the inlet turbulence intensity I_{in} was tested. Fig. 2 shows the variations of cross-sectional area-averaged turbulence intensity ($I = \sqrt{(2/3)k_{\mathrm{mean}}/u_{\mathrm{in}}^2}$) and pressure drop Δp ($\Delta p = \bar{p} - p_{\mathrm{in}}$) as a function of the axial distance from the mouth inlet for an inspiratory flow rate of $Q_{\mathrm{in}} = 30$ l/min, with different assumed inlet turbulence intensities. For a very low inlet turbulence intensity ($I_{\mathrm{in}} = 0.01$), the onset of turbulence occurs only after the glottis. The variation of turbulence intensity after the soft palate is essentially independent of its inlet values if $I_{\mathrm{in}} \geqslant 0.037$. The assumed inlet turbulence intensity has negligible effects on the mean flow fields in the tubular airways. No-slip conditions were employed at the airway walls. Particle deposition occurs when its center comes within a radius from the wall, i.e., particles adhere as soon as they touch the wall, which is a realistic assumption.

2.2. Numerical method

The numerical solutions of the continuity and momentum equations as well as the k and ω equations were carried out with a user-enhanced commercial finite-volume based program, i.e., CFX4.4 from AEA Technology (2001). The numerical program uses a structured, multiblock,

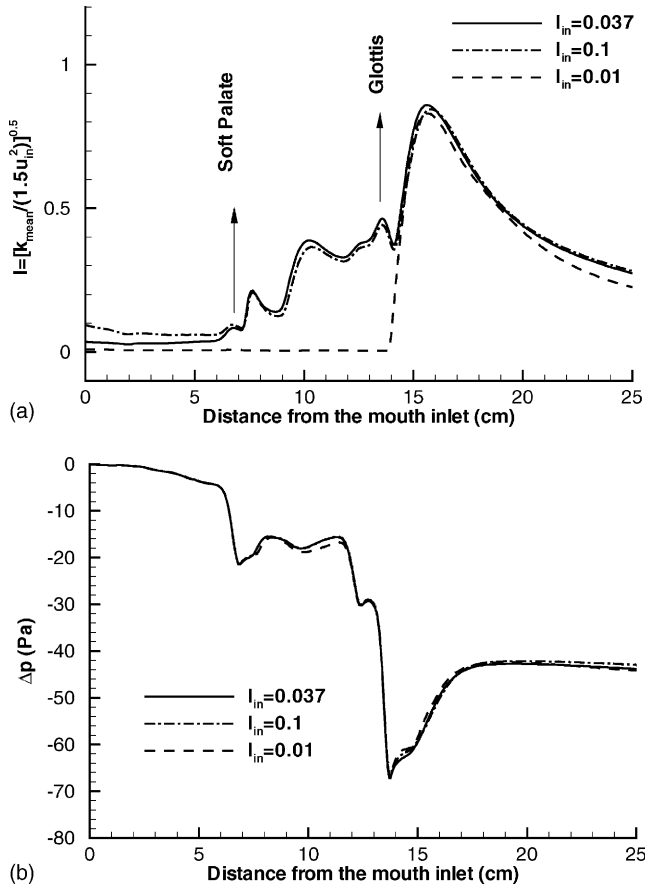

Fig. 2. Variations of: (a) cross-sectional area-averaged turbulence intensities; and (b) pressure drops in the oral airway model for $Q_{in} = 30$ l/min.

body-fitted coordinate discretization scheme. In the present simulation, the PISO algorithm with under-relaxation was employed to solve the flow equations. All variables, including velocity components, pressure, and turbulence quantities, are located at the centroids of the control volumes. An improved Rhie–Chow interpolation method was employed to obtain the velocity components, pressure and turbulence variables on the control volume faces from those at the control volume centers. A higher-order upwind differencing scheme, which is second-order accurate in space, was used to model the advective terms of the transport equations. The sets of linearized and discretized equations for all variables were solved using the Block Stone's method.

The particle transport equation was also solved with the commercial software in combination with user-specified drag relations and detailed particle tracking. After the constant flow field has been established, particles were released simultaneously at the mouth inlet. The air flow fluctuations were modeled with Eq. (10), which is assumed to be independent of time. In CFX, the equations for particle trajectories were solved using Gear's BDF method. After each iteration for each particle, the information about position, time, and three components of the velocity as well

as the speed with which the particles cross the control volume boundaries was obtained. A user-specified near-wall particle tracking program was used to calculate the distances from the particle centers to the wall to find out if the particles deposit. In the current model the number of particles, about 10,000, was determined by increasing the inlet particle concentration until the deposition fraction became independent of the number of particles simulated. The deposition fraction is defined as the ratio of the number of particles deposited in the oral airway to the total number entering at the mouth.

The computational mesh (cf. Fig. 3) was generated with CFX Build4 where each control volume (mesh element) is an irregular hexahedron defined by its eight vertices. The near-wall region required a very dense mesh. Specifically, the thickness of the near-wall cells was chosen to fully contain the viscous sub-layers and to resolve any geometric features present there. As a requirement of LRN turbulence modeling, the first grid point above the wall was given a value of $y^+ \leqslant 1$, where $y^+ = u_\tau y/v$ is the inner variable or sub-layer-scaled distance, and this criterion is strictly maintained for all computations. The mesh topology was determined by refining the mesh until grid independence of the flow field solution was achieved. The final mesh contains about 640,000 cells. The computations were performed on an SGI Origin 2400 workstation with 32GB RAM and multiple 450 MHz CPUs. The steady-state solution of the flow field was assumed converged when the dimensionless mass residual, (Total Mass Residual)/(Mass Flow Rate) $< 10^{-3}$. The convergence of k and ω was monitored as well. Typical run time for the fluid flow simulations on four processors with parallel algorithm was approximately 40–50 h. Utilizing the

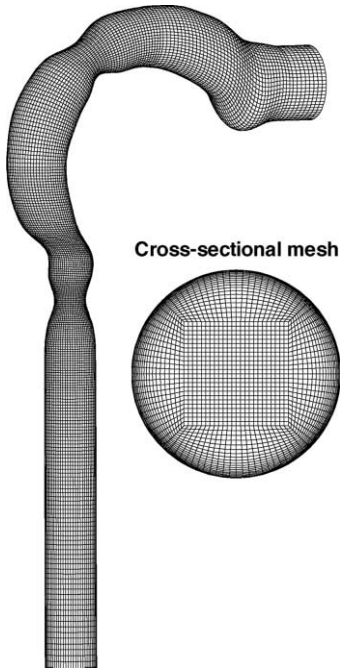

Fig. 3. Finite-volume mesh of the oral airway model.

converged flow field solution, the particle trajectory simulations required approximately 4–6 h for each Stokes number considered.

2.3. Model validation

The present computational fluid-particle dynamics model has been validated with various experimental data sets for steady and transient laminar flows in bifurcations (Comer et al., 2000, 2001; Zhang and Kleinstreuer, 2002b; Zhang et al., 2002) and for laminar, transitional and turbulent flows in tubes with local obstructions (Zhang and Kleinstreuer, 2002a). Similarly, micron-particle depositions in airways were successfully compared with measured deposition efficiencies and deposition patterns (cf. Comer et al., 2000; Zhang et al., 2002). Fig. 4 depicts a comparison of the present deposition efficiency results with the experimental correlation of Cheng et al. (1999) for similar inlet Reynolds numbers. The Stokes number is defined here as by Cheng et al. (1999), i.e., $St = \rho_p d_p^2 U/9\mu D$, with U being the mean-velocity evaluated as (Q/A), where A is the mean cross-sectional area and D is the minimum hydraulic diameter. Clearly, our computational data points nicely retrace the correlated curve of measured deposition data. It also indicates that the present modeling of particle deposition in the oral airways with the LRN k–ω model and the corresponding particle dispersion model is more accurate than the previous studies with k–ε models which may predict the deposition efficiency 200% higher than the experimental values (Stapleton et al., 2000).

In summary, the good agreements between experiments and predictions instill confidence that the present computer simulation model is sufficiently accurate to analyze laminar-to-turbulent fluid-particle dynamics in a three-dimensional tubular airway.

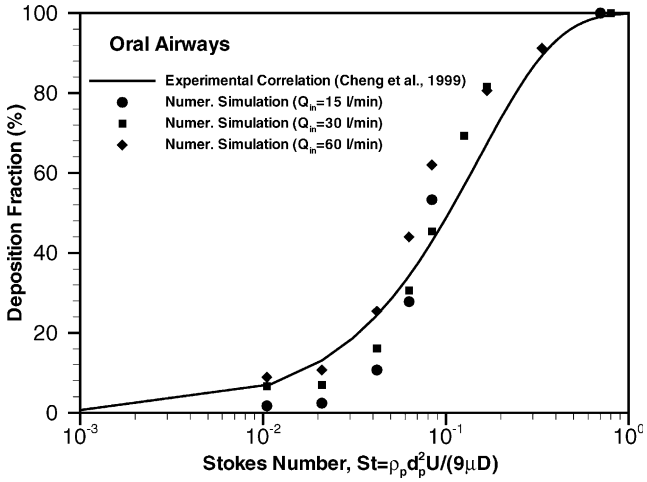

Fig. 4. Comparison of simulated particle deposition fractions in the oral airway model with the experimental data correlation of Cheng et al. (1999). The particle deposition fraction is defined as the ratio of the number of particles deposited at the oral airway to the total number entering.

3. Results and discussion

3.1. Airflow structures

The oral airway (Fig. 1) is representative of complex tubular systems and hence the effects of local turbulence at different flow rates on the airflow structure and particle transport can be nicely illustrated. Fig. 5 shows the mean-velocity fields in the oral airway model with an inspiratory flow rate of $Q_{in} = 15$ l/min, i.e., low-level breathing. The cross-sectional views display the axial velocity contours as well as secondary velocity vectors. The cross-sections C–C′, D–D′, E–E′ and F–F′ are zero, one, three, and six diameter(s) from the glottis, respectively. The primary characteristics of the axial flow fields are: (i) skewed velocity profiles with the maximum velocity shifted to the outer bend generated by the centrifugal force in the curved portion from the oral cavity to the pharynx/larynx; (ii) recirculation zones due to abrupt geometric changes, i.e., the variation of cross-sectional area in the lower portion of the mouth (near the tongue), the inside bend of the pharynx

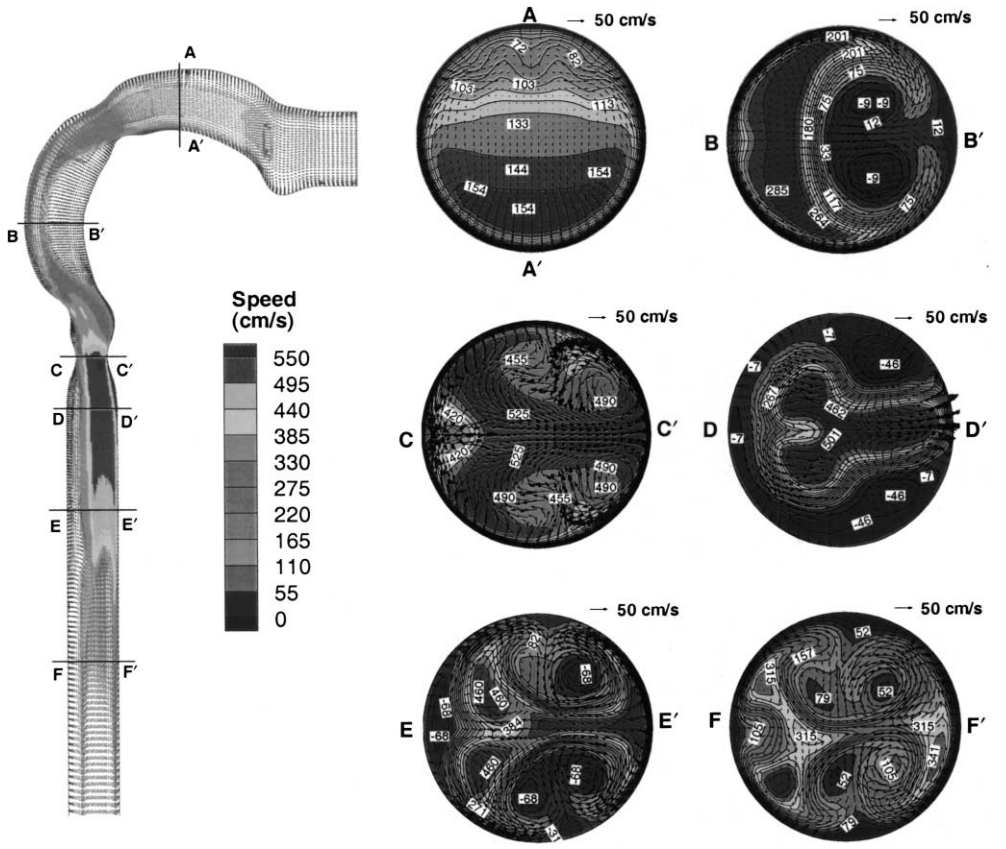

Fig. 5. Velocity profiles in the oral airway model at $Q_{in} = 15$ l/min. The left panel exhibits mid-plane ($y = 0$ plane) velocity contours with uniform velocity vectors. The right panel shows the axial velocity contours (magnitudes in cm/s) and secondary velocity vectors at different cross-sections.

(B–B′), and downstream of the vocal fold (glottis); and (iii) an asymmetric, central jet created by the restriction of the vocal folds. Secondary motion is set up when the flow turns a bend from the mouth to the pharynx because of the centrifugally induced pressure gradient. Secondary flows become more and more complicated downstream from the mouth when the air stream encounters expansion or constriction with the variation of cross-sectional areas and continue to turn a bend from the pharynx to the larynx. In addition, the interaction between secondary and axial motion also causes more complicated flows, e.g., six distinct vortices can be observed at cross-section F–F′.

When the shallow inspiratory flow rate is, say, $Q_{in} = 15$ l/min, the turbulence intensity is very low (cf. Fig. 6), and the maximum k/u_{in}^2-value is less than 0.002, i.e., equal to the given turbulence kinetic energy at the inlet, which indicates that the inlet turbulence is damped out and laminar flow prevails under such a low flow rate condition. This inhalation scenario clearly demonstrates the importance of laminar flow simulation with a LRN turbulence model.

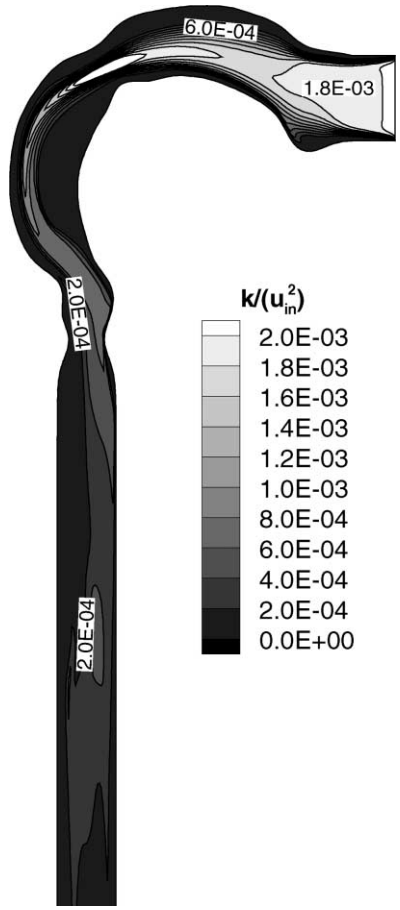

Fig. 6. Distribution of turbulence kinetic energy (k/u_{in}^2) in the oral airway model ($y = 0$ plane) at $Q_{in} = 15$ l/min.

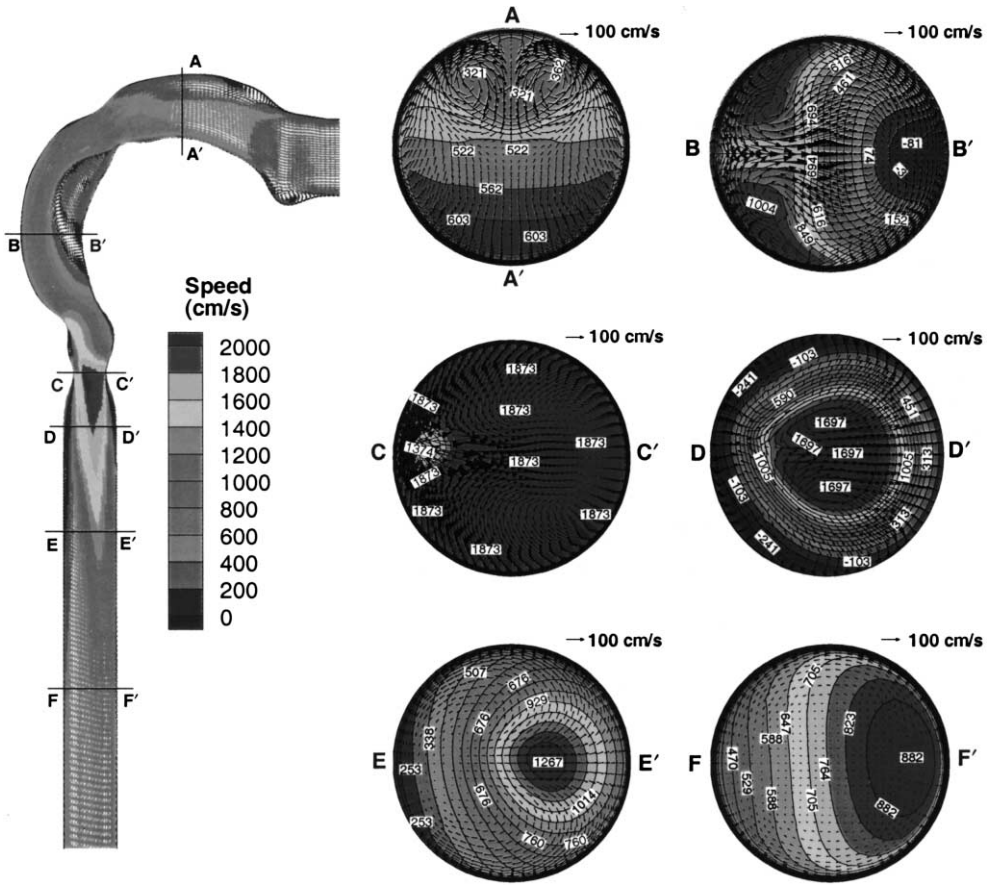

Fig. 7. Velocity profiles in the oral airway model at $Q_{in} = 60$ l/min. The left panel exhibits mid-plane ($y = 0$ plane) velocity contours with uniform velocity vectors. The right panel shows the axial velocity contours (magnitudes in cm/s) and secondary velocity vectors at different cross-sections.

When the inspiratory flow rate is dramatically increased to 60 l/min, i.e., exercise breathing, the velocity profiles (Fig. 7) and the turbulence energy profiles (Fig. 8) change measurably. The velocity profiles in the initial parts of the oral airway (cf. cross-section A–A′) are similar to those for $Q_{in} = 15$ l/min except for the increase of secondary motion and two secondary vortices appearing at A–A′. Turbulence fluctuations are still weak in this part. But after the soft palate (cf. Fig. 1), the situation changes significantly because of the occurrence of transition to turbulence. Both axial and secondary flows are influenced by the onset of turbulence. The length of the separated flow zone after the glottis also decreases compared to that for the lower flow rate case (Figs. 5 and 6). For example, there is no reverse flow at cross-section E–E′ (three diameters downstream of the glottis) for $Q_{in} = 60$ l/min while it still appears for the $Q_{in} = 15$ l/min case. This may be because the occurrence of transition to turbulence in the downstream regions of the shear layer modifies the location of reattachment compared with that for laminar flow (cf. Ahmed and Giddens, 1983). With further redistribution of the kinetic energy of the flow over most of the cross-section, the

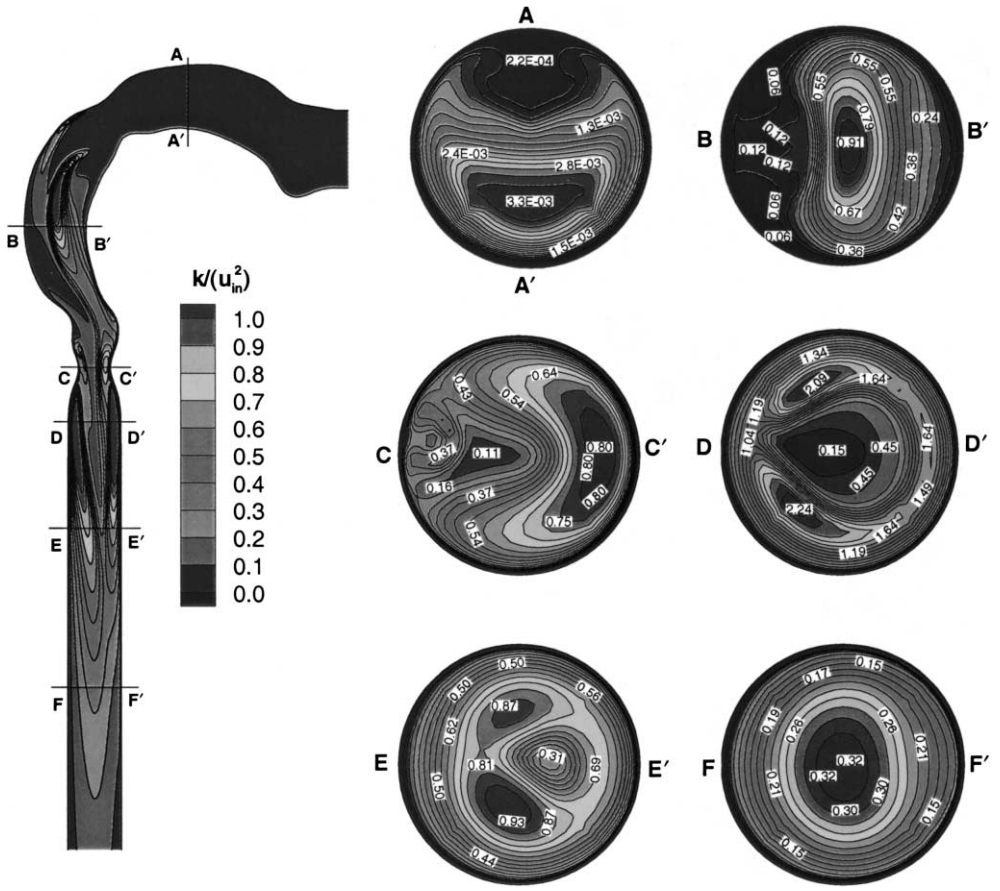

Fig. 8. Distribution of turbulence kinetic energy (k/u_{in}^2) in the oral airway model at $Q_{in} = 60$ l/min. The left panel is the side-view ($y = 0$ plane) and the right panel provides the cross-sectional views.

velocity profiles become more blunt from the left to the right wall, and the maximum velocity zone moves to the anterior wall (F′) at the cross-section F–F′ (six diameters from the glottis). The secondary motion decays and appears very weak at this cross-section. Fig. 8 shows that the turbulence kinetic energy becomes strong after the constriction caused by the soft palate, and then decays until the disturbance is activated again by the throat (glottis). The maximum turbulence fluctuations occur in the shear layer rather than along the centerline after the glottis. This phenomenon indicates that the flow first becomes unstable in the region of the shear layer bounding the jet emerging from the throat (cf. Yongchareon and Young (1979)). Similar patterns of axial turbulence intensity were measured and reported by Corcoran and Chigier (2000) and Gemci et al. (2002). High-levels of turbulence intensity can be observed in Fig. 8 near the posterior/left and posterior/trachea wall from 0.5 to 2.0 diameters downstream of the glottis. This is similar to some experimental results. For example, the measurements of Corcoran and Chigier (2000) show for the laryngeal jet that the maximum turbulence intensity occurs 0.5 to 1 diameter downstream of the

throat. Ahmed and Giddens (1983) recorded the maximum turbulence fluctuations at about 3.5 diameters from the throat in a smoothly constricted tube. The variation in the location of maximum turbulence intensity may be attributed to geometric characteristics (e.g., bend, area reduction, etc.) and the shape of the constrictions. A general trend in turbulence generation and decay is apparent as reported in experimental studies (Ahmed and Giddens, 1983; Corcoran and Chigier, 2000). Turbulence levels appear to increase quickly in the region 0–2.5 diameters after the glottis, and then decay approaching an asymptotic level of approximately 0.2–0.3 at 6 diameters from the throat (cross-section F–F′). This is also consistent with the statement given by Chang (1989) based on their experimental studies concerning the effect of the larynx, i.e., the larynx has no significant effect on the velocity profiles beyond the carina over the entire inspiratory phase of the respiratory cycle.

It is interesting to note that the axial velocity contours, secondary motions, as well as trends in turbulence generation and decay for the strong breathing mode ($Q_{in} = 60$ l/min) (cf. Figs. 7 and 8) resemble those for $Q_{in} = 30$ l/min, i.e., light activity breathing. The slight difference is that the maximum turbulence in the trachea is closer to the throat for the $Q_{in} = 60$ l/min case and that the turbulence levels decay faster for the higher flow rate case. As a result, the maximum

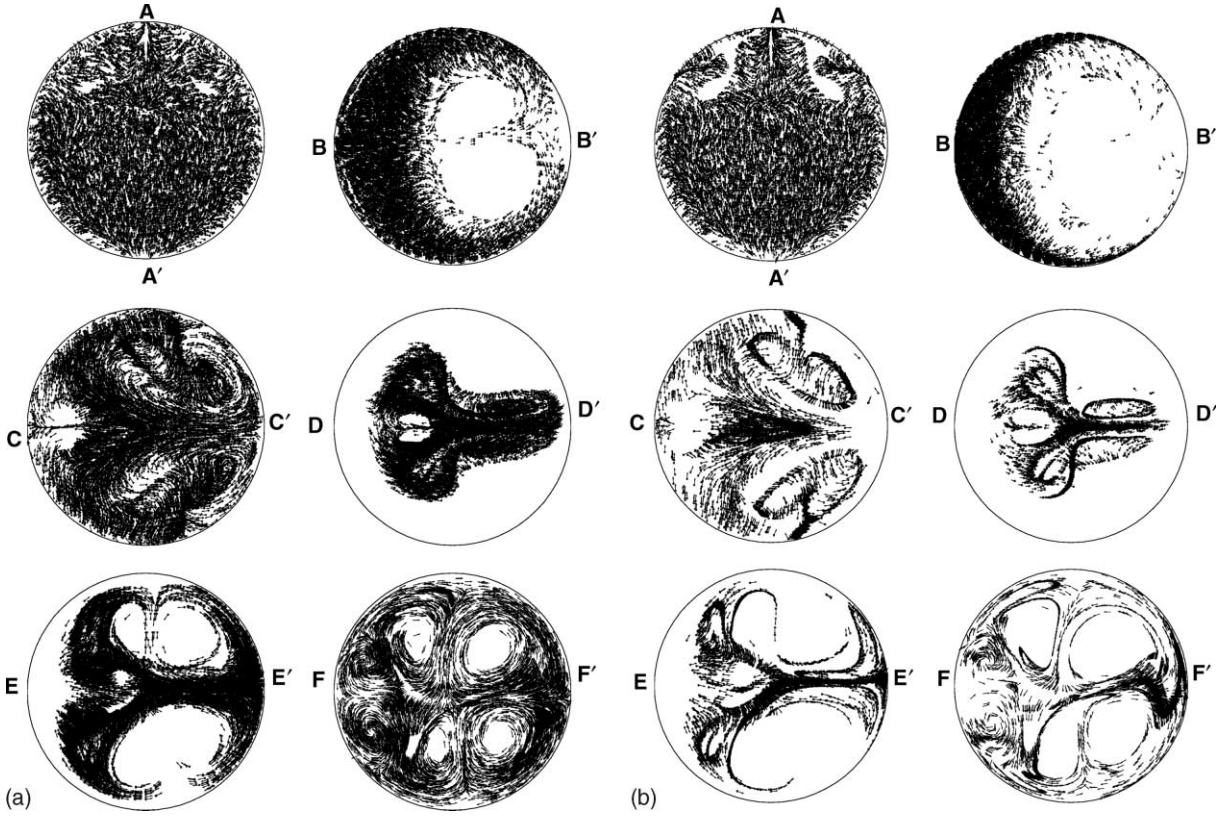

Fig. 9. Particle distributions and flow directions in the oral airway model for: (a) $Q_{in} = 15$ l/min, $St = 0.02$; and (b) $Q_{in} = 15$ l/min, $St = 0.08$.

k/u_{in}^2-values at cross-sections E–E′ and F–F′ are lower for the $Q_{in} = 60$ l/min case when compared to the 30 l/min case. The same phenomenon was reported experimentally by Corcoran and Chigier (2000). They found that the turbulence levels were approximately 20% higher at the furthest downstream locations for their $Re = 1250$ case when compared to the $Re = 2800$ case. This is likely due to the complex nature of the confined jet flow. The higher Reynolds number jet expands more quickly and transports more momentum to the flow downstream of the throat creating similar axial velocity conditions and potentially lower turbulence intensities (cf. Corcoran and Chigier, 2000).

3.2. Particle motion

Cross-sectional particle distributions in sequence are useful to illustrate the interaction of airflow structures and particle suspension flow, and hence to elucidate physical insight of particle deposition. Particle distributions and directional arrows from cross-section A–A′ to F–F′ are shown in Figs. 9 and 10, for the flow fields depicted in Figs. 5 and 7, respectively. For a given cross-section, the particle distribution was captured just when these particles passed through this

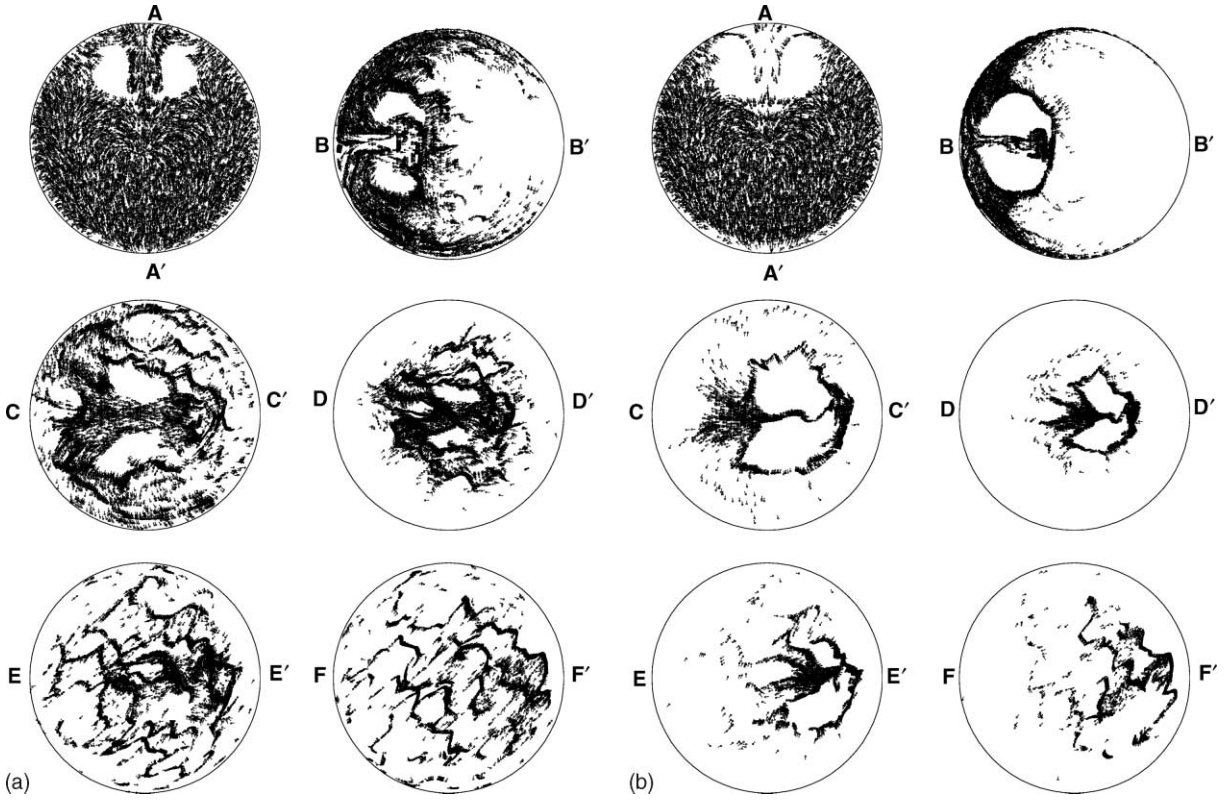

Fig. 10. Particle distributions and flow directions in the oral airway model for: (a) $Q_{in} = 60$ l/min, $St = 0.02$; and (b) $Q_{in} = 60$ l/min, $St = 0.08$.

section. For each inhalation flow rate, two Stokes numbers (i.e., $St = 0.02$ and 0.08) were considered. As shown in Fig. 7 for the lower flow rate ($Q_{in} = 15$ l/min), particles follow the basic relationship between airflow and particle motion very well without the onset of turbulence, which was also observed for laminar flow in bifurcating airways (cf. Zhang et al., 2001; Zhang and Kleinstreuer, 2002a). Specifically, the axial flow is the indicator of the concentration of particle distribution. For example, at cross-section D–D′, particles concentrate at the high axial velocity zone, and no particles accumulate in the reversed flow zone. Particles essentially follow the secondary motion; however, particles may be expelled from the vortex centers, generating distinct

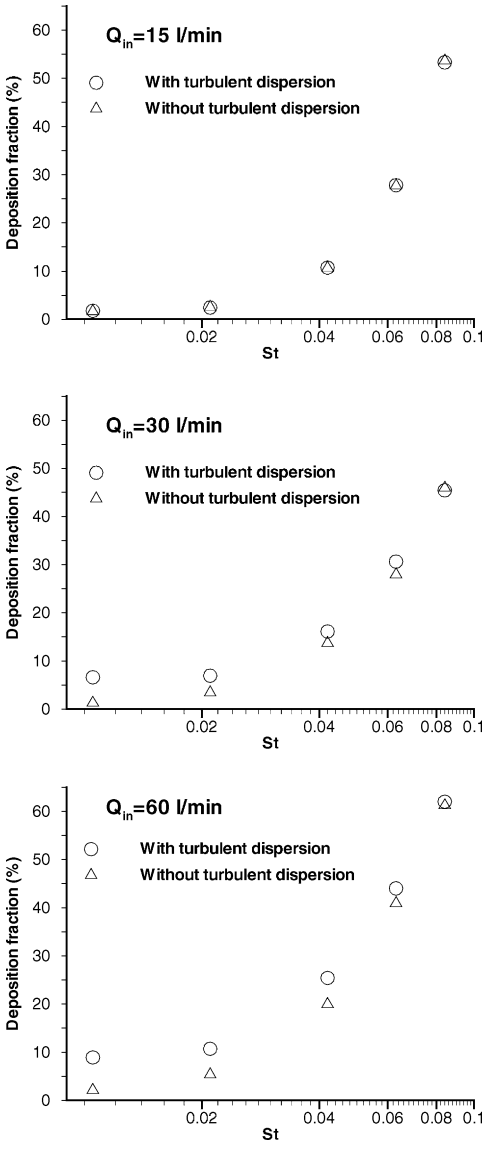

Fig. 11. Effect of turbulent dispersion on particle deposition fractions for different inspiratory flow rates.

particle-free zones in the tube (cf. Sections B–B′, E–E′, F–F′) associated with the high intensity of secondary flow. In other words, particles entrained by an eddy will tend to move towards regions of high shear and low vorticity, i.e., along the vortex edges (cf. Longmire and Eaton, 1992). Such distinct particle-free zones in the trachea have a profound effect on particle deposition sites and concentrations further downstream in the lung.

Comparing Fig. 9(a) with (b), the Stokes number effect becomes apparent. With an increase in Stokes number, more particles may impact and deposit in the mouth/pharynx/larynx region due to the high inertia force, i.e., fewer particles can reach the trachea (cf. cross-sections C–C′ to F–F′ in Fig. 9(b)). At the same time, with increasing Stokes number, the centrifugal force increases and the particle void regions become larger.

With high inspiratory flow rates, particle flow fields (cf. Fig. 10) in the initial parts of the oral airways, i.e., upstream of the soft palate, are similar to those at the low flow rate (cf. cross-sectional views in A–A, B–B′) with low turbulence levels. After the soft palate, however, particle motion seems to be random and disperse, i.e., influenced by the flow fluctuations with the onset of turbulence (cf. Sections C–C′ to F–F′ in Fig. 10). Specifically, particle distributions become very complex and random in the trachea with the high-levels of turbulence after the glottis. Turbulence dispersion plays a significant role for particle motion in the trachea. Because the seed for generating the random number which simulate the fluctuation of the airflow (cf. Eq. (10)) is the same for all cases presented here, the random motion of particles seems similar for the two cases depicted in Fig. 10(a) and (b). In any case, from the point of statistics and stochastics, this should

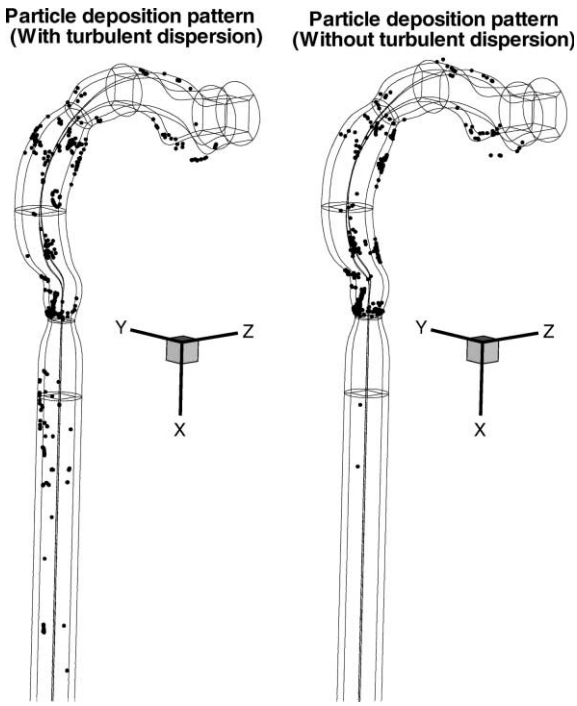

Fig. 12. Particle deposition patterns in the oral airway model for $Q_{in} = 30$ l/min and $St = 0.02$.

not influence the particle *deposition* because enough particles were released at the inlet and the selection of seeds was examined in prior test runs.

3.3. Effects of turbulent dispersion

As mentioned, the particle motion in the trachea may appear to be random due to turbulent air fluctuations. How does turbulence affect the particle deposition fraction in the oral airway? In a detailed evaluation, Fig. 11 shows the particle deposition fraction vs. typically low Stokes numbers for three inspiratory flow rates with turbulent dispersion as a parameter. As expected, there is no turbulent dispersion effect for the low inspiratory flow rate case ($Q_{in} = 15$ l/min). Particle deposition is enhanced by turbulence at $Q_{in} = 30$ and 60 l/min when $St \leqslant 0.06$. The turbulence effect becomes small for high Stokes numbers because many particles deposit upstream and the heavy particles are not influenced by airflow fluctuations. The comparison of the local deposition patterns with and without turbulent dispersion in the oral airway is shown in Fig. 12. Clearly, turbulence measurably enhances particle deposition in the trachea. Schlesinger and Lippman (1976) also reported that turbulence is more likely to affect the deposition of smaller particles in the trachea.

4. Conclusions

The laminar-to-turbulent fluid-particle dynamics in a human oral airway model has been investigated numerically for different steady inspiratory flow rates and Stokes numbers, employing an LRN k–ω turbulence model and proper particle trajectory simulation. The 3-D simulation results show the following:

(i) The onset of turbulence after the glottis can be clearly observed when the inspiratory flow rate changes from low-level breathing ($Q_{in} = 15$ l/min) to strong breathing ($Q_{in} = 60$ l/min). The flow reattachment length in the trachea becomes shorter, the axial velocity profile becomes more blunt, and the secondary flow decays faster, due to the redistribution of the kinetic energy with the occurrence of transition to turbulence. However, both the velocity profiles and the turbulence energy profiles vary little when the inspiratory flow rate changes from 30 l/min (light activity breathing) to 60 l/min (exercise breathing). The downstream turbulence intensity in the trachea which may be propagated to the bronchial airway is slightly lower with an inspiratory flow rate of 60 l/min.

(ii) Particles follow the basic relationship between airflow and particle motion very well at the lower inspiratory flow rate ($Q_{in} = 15$ l/min); however, particle motion seems to be random and disperse, i.e., influenced by flow fluctuations in case of the high inspiratory flow ($Q_{in} = 60$ l/min).

(iii) Turbulence can enhance particle deposition in the trachea near the larynx to some extent, but it is more likely to affect the deposition of smaller particles (say, $St < 0.06$) throughout the airway for relatively high flow rates ($Q_{in} = 30$ and 60 l/min) due to turbulent dispersion. However, the particle size and inhalation flow rate (i.e., Stokes number) are still the main factors influencing particle deposition when compared with turbulent dispersion alone.

Although the present oral airway geometry is relatively simple compared with the cast model (Cheng et al., 1999), it considers the key dimensions and the critical geometry features depicted by cast models, and it can generate the equivalent filtering efficiency (i.e., comparable deposition fractions) for micron-size particles as shown with complicated cast models (Cheng et al., 1999). Therefore, the present simulation should exhibit the main features of the laminar–transitional–turbulent air/particle flows in realistic human oral airways and may serve as a model for other internal two-phase flow systems.

The effects of the shape of the glottis which may cause the downstream velocity profiles to rotate to some degree and may have a minor effect on downstream turbulence intensity, as well as effects of different openings of the glottis associated with the inspiratory flow rates will be investigated in the future.

Disclaimer: The views and conclusions contained herein are those of the authors and should not be interpreted as necessarily representing the official policies or endorsements, either expressed or implied, of the Air Force Office of Scientific Research or the US Government.

Acknowledgements

This effort was sponsored by the Air Force Office of Scientific Research, Air Force Material Command, USAF, under grant number F49620-01-1-0492 (Dr. Walt Kozumbo, Program Manager) and the National Science Foundation (BES-0201271; Dr. Gil Devey, Program Director). The US Government is authorized to reproduce and distribute reprints for governmental purposes notwithstanding any copyright notation thereon. The use of CFX software from AEA Technology (Pittsburgh, PA) and access to the SGI Origin 2400 workstation at the North Carolina Supercomputing Center (Research Triangle Park, NC) are gratefully acknowledged as well.

References

AEA Technology, 2001. CFX-4.4: Solver. CFX International, Oxfordshire, UK.

Ahmed, S.A., Giddens, D.P., 1983. Velocity measurements in steady flow through axisymmetric stenoses at moderate Reynolds number. J. Biomechanics 16, 505–516.

Berger, S.A., Jou, L.D., 2000. Flows in stenotic vessels. Annu. Rev. Fluid Mech. 32, 347–382.

Chang, H.K., 1989. Flow dynamics in the respiratory tract. In: Chang, H.K., Paiva, M. (Eds.), Respiratory Physiology: An Analytical Approach. Marcel Dekker Inc., New York, pp. 57–138.

Cheng, Y.S., Zhou, Y., Chen, B.T., 1999. Particle deposition in a cast of human oral airways. Aerosol Sci. Technol. 31, 286–300.

Clift, R., Grace, J.R., Weber, M.E., 1978. Bubbles, Drops, and Particles. Academic Press, NY.

Comer, J.K, Kleinstreuer, C., Hyun, S., Kim, C.S., 2000. Aerosol transport and deposition in sequentially bifurcating airways. ASME J. Biomechanical Eng. 122, 152–158.

Comer, J.K., Kleinstreuer, C., Zhang, Z., 2001. Flow structures and particle deposition patterns in double bifurcation airway models. Part 1. Air flow fields. J. Fluid Mech. 435, 25–54.

Corcoran, T.E., Chigier, N., 2000. Characterization of the laryngeal jet using phase doppler interferometry. J. Aerosol Med. 13, 125–137.

Gemci, T., Corcoran, T.E., Chigier, N., 2002. A numerical and experimental study of spray dynamics in a simple throat model. Aerosol Sci. Technol. 36, 18–38.

Gosman, A.D., Ioannides, E., 1981. Aspects of computer simulation of liquid-fueled combustors. J. Energy 7, 482–490.
Katz, I.M., Martonen, T.B., 1996. Flow patterns in three-dimensional laryngeal models. J. Aerosol Med. 9, 501–512.
Katz, I.M., Martonen, T.B., 1999. A numerical study of particle motion within the human larynx and trachea. J. Aerosol Sci. 30, 173–183.
Kral, L.D., 1998. Recent experience with different turbulence models applied to the calculation of flow over aircraft components. Prog. Aerospace Sci. 34, 481–541.
Ku, D.N., 1997. Blood flow in arteries. Annu. Rev. Fluid Mech. 29, 399–434.
Li, W.I., Perzl, M., Heyder, J., Langer, R., Brain, J.D., Englmeier, K.H., Niven, R.W., Edwards, D.A., 1996. Aerodynamics and aerosol particle deaggregation phenomena in model oral–pharyngeal cavities. J. Aerosol Sci. 27, 1269–1286.
Li, W.I., Perzl, M., Ferron, G., Batycky, R., Heyder, J., Edwards, D.A., 1998. The macrotransport properties of aerosol particles in the human oral–pharyngeal region. J. Aerosol Sci. 29, 995–1010.
Longmire, E.K., Eaton, J.K, 1992. Structure of a particle-laden round jet. J. Fluid Mech. 236, 217–257.
Molerus, O., 1996. Overview: pneumatic transport of solids. Powder Technol. 88, 309–321.
Papageorgakis, G.C., Assanis, D.N., 1999. Comparison of linear and nonlinear RNG-based k–ε models for incompressible turbulent flows. Numer. Heat Transfer Part B 35, 1–22.
Pope, S.B., 2000. Turbulent Flows. Cambridge University Press, Cambridge, United Kingdom.
Radmehr, A., Patankar, S.V., 2001. Computation of boundary layer transition using low-Reynolds-number turbulence models. Numer. Heat Transfer 39, 525–543.
Schlesinger, R.B., Lippman, M., 1976. Particle deposition in the trachea: in vivo and in hollow casts. Thorax 31, 678–684.
Stapleton, K.W., Guentsch, E., Hoskinson, M.K., Finlay, W.H., 2000. On the suitability of k–ε turbulence modeling for aerosol deposition in the mouth and throat: a comparison with experiment. J. Aerosol Sci. 31, 739–749.
Wilcox, D.C., 1998. Turbulence Modeling for CFD, second ed DCW Industries Inc., LA Canada, CA.
Yongchareon, W., Young, D.F., 1979. Initiation of turbulence in models of arterial stenoses. J. Biomechanics 12, 185–196.
Yu, G., Zhang, Z., Lessmann, R., 1998. Fluid flow and particle diffusion in the human upper respiratory system. Aerosol Sci. Technol. 28, 146–158.
Zhang, Z., Kleinstreuer, C., 2002a. Modeling of low Reynolds number turbulent flows in locally constricted conduits: a comparison study. AIAA J. (in press).
Zhang, Z., Kleinstreuer, C., 2002b. Transient airflow structures and particle transport in a sequentially branching lung airway model. Phys. Fluids 14, 862–880.
Zhang, Z., Kleinstreuer, C., Kim, C.S., 2001. Flow structure and particle transport in a triple bifurcation airway model. J. Fluids Eng.-Trans. ASME 123, 320–330.
Zhang, Z., Kleinstreuer, C., Kim, C.S., 2002. Cyclic micron-size particle inhalation and deposition in a triple bifurcation lung airway model. J. Aerosol Sci. 33, 257–281.